

# *Shear-induced electrical changes in the base of thin layer cloud*

Article

Accepted Version

Harrison, G. ORCID: <https://orcid.org/0000-0003-0693-347X>, Marlton, G., Aplin, K. L. and Nicoll, K. A. ORCID: <https://orcid.org/0000-0001-5580-6325> (2019) Shear-induced electrical changes in the base of thin layer cloud. Quarterly Journal of the Royal Meteorological Society, 145 (725). pp. 3667-3679. ISSN 1477-870X doi: <https://doi.org/10.1002/qj.3648> Available at <https://centaur.reading.ac.uk/86102/>

It is advisable to refer to the publisher's version if you intend to cite from the work. See [Guidance on citing](#).

To link to this article DOI: <http://dx.doi.org/10.1002/qj.3648>

Publisher: Royal Meteorological Society

All outputs in CentAUR are protected by Intellectual Property Rights law, including copyright law. Copyright and IPR is retained by the creators or other copyright holders. Terms and conditions for use of this material are defined in the [End User Agreement](#).

[www.reading.ac.uk/centaur](http://www.reading.ac.uk/centaur)

**CentAUR**

Central Archive at the University of Reading

Reading's research outputs online

**Shear-induced electrical changes in the base of thin layer-  
cloud**

Journal:	<i>QJRMS</i>
Manuscript ID	QJ-18-0181.R2
Wiley - Manuscript type:	Research Article
Date Submitted by the Author:	01-Aug-2019
Complete List of Authors:	Harrison, Giles; University of Reading, Department of Meteorology Marlton, Graeme; University of Reading, Department of Meteorology Aplin, Karen; University of Oxford, Physics; University of Bristol, Aerospace Engineering Nicoll, Keri; University of Reading, Department of Meteorology
Keywords:	atmospheric electricity, stratiform cloud, Kelvin-Helmholtz billows, cloud microphysics
Country Keywords:	United Kingdom Of Great Britain And Northern Ireland

# Shear-induced electrical changes in the base of thin layer-cloud

R. Giles Harrison<sup>1</sup>, Graeme J. Marilton<sup>1</sup>, Karen L. Aplin<sup>2</sup>, Keri A. Nicoll<sup>1,3</sup>

<sup>1</sup> Department of Meteorology, University of Reading, UK

<sup>2</sup> Department of Physics, University of Oxford, UK, *now at* Department of Aerospace Engineering, University of Bristol, UK

<sup>3</sup> Department of Electronic and Electrical Engineering, University of Bath, UK

## Abstract

Charging of upper and lower horizontal boundaries of extensive layer clouds results from current flow in the global electric circuit. Layer-cloud charge accumulation has previously been considered a solely electrostatic phenomenon, but it does not occur in isolation from meteorological processes, which can transport charge. Thin layer clouds provide special circumstances for investigating this dynamical charge transport, as disruption at the cloud-top may reach the cloud base, observable from the surface. Here, a thin (~300 m) persistent layer-cloud with base at 300 m and strong wind shear at cloud-top was observed to generate strongly correlated fluctuations in cloud base height, optical thickness and surface electric Potential Gradient (PG) beneath. PG changes are identified to precede the cloud base fluctuations by 2 minutes, consistent with shear-induced cloud-top electrical changes followed by cloud base changes. These observations demonstrate, for the first time, dynamically driven modification of charge within a layer-cloud. Even in weakly charged layer-clouds, redistribution of charge will modify local electric fields within the cloud and the collisional behaviour of interacting charged cloud droplets. Local field intensification may also explain previously observed electrostatic discharges in warm clouds.

*Keywords:* atmospheric electricity; stratiform cloud; Kelvin-Helmholtz billows; cloud microphysics;

## 1. Introduction

Stratiform clouds cover about 40% of the planet (Klein and Hartman, 1993), and have an important role in the radiation balance, which is strongly influenced by cloud microphysical properties such as the droplet size distribution. For horizontally extensive layer-clouds, such as those providing whole

1  
2  
3 31 sky coverage as seen from a particular observing site, the cloud acquires electric charge at its upper  
4  
5 32 and lower horizontal boundaries. Acquisition of charge at the cloud boundary results from current  
6  
7 33 flowing in the global atmospheric electric circuit, through which charge transfer occurs between  
8  
9 34 thunderstorm regions and distant regions of undisturbed weather. Charging of small droplets has  
10  
11 35 been suggested to influence their behaviour through modifying collision (Tinsley *et al* 2000; Khain *et*  
12  
13 36 *al* 2004) and activation (Harrison and Ambaum 2008) processes. Clear evidence for upper and lower  
14  
15 37 edge electrification (of positive and negative charge respectively) has now been obtained at multiple  
16  
17 38 sites using instrumented balloon soundings (Nicoll and Harrison, 2016), and charging of the lower  
18  
19 39 boundary has also been found to be directly observable from surface sensors, if the cloud base is  
20  
21 40 below 1500 m (Harrison *et al*, 2017a).

22  
23  
24  
25  
26 41 Previous work on layer-cloud charging has concentrated on a decoupled electrostatic  
27  
28 42 representation, assuming the cloud is meteorologically passive (e.g. Zhou and Tinsley 2012).  
29  
30 43 Observations (Nicoll and Harrison, 2016) show that, whilst the straightforward electrostatic  
31  
32 44 description of upper edge positive charge and lower edge negative charge does emerge on average,  
33  
34 45 individual layer-clouds show substantial variability with charge present throughout the vertical  
35  
36 46 extent of the cloud as well as at the upper and lower edges. There are several possible reasons for  
37  
38 47 this, at least two of which are meteorological in origin. Firstly, the cloud boundary properties depend  
39  
40 48 on the local meteorological conditions, through the effect of the temperature inversion at the cloud-  
41  
42 49 top and updraft strength at the cloud base. These influence the vertical electrical conductivity  
43  
44 50 gradient at each horizontal cloud boundary and, in turn, the cloud edge charge (Nicoll and Harrison,  
45  
46 51 2016). Secondly, mixing and turbulence occur within layer-clouds (Shao *et al*, 1997), which  
47  
48 52 transports charge from the edge region into the main body of the cloud. A purely electrostatic model  
49  
50 53 can therefore only provide an approximate representation of layer-cloud electrification, particularly  
51  
52 54 if based on simple geometry, as the charges generated at the cloud edges are always susceptible to  
53  
54 55 dynamical transport and turbulent mixing processes.  
55  
56  
57  
58  
59  
60

1  
2  
3 56 In this paper, above-cloud instability is shown to influence the charged regions within a thin but  
4  
5 57 persistent low level extensive layer-cloud. Remote electrostatic sensing is used to investigate  
6  
7 58 fluctuations in the charged cloud base and the effect of enforced motion disturbing charge at the  
8  
9 59 upper cloud edge is explored.

## 60 2. Meteorological circumstances

### 61 (a) Instrumentation

62 The vertical electric Potential Gradient (PG) at the surface<sup>1</sup> is a widely observed property in  
63 atmospheric electricity, and shows appreciable variability on many timescales from minutes to days  
64 arising from weather, space weather and air pollution changes (Harrison and Nicoll, 2018). In the  
65 specific circumstances of persistent layer-clouds with a cloud base below about 1500 m,  
66 Harrison et al (2017a) demonstrated that cloud base charge influences the PG measured at the  
67 surface. As the cloud base lowers, the surface PG is reduced by the increasing proximity of negative  
68 charge in the cloud base. For these studies the surface PG was obtained using an upwards-facing  
69 field mill, and the cloud base height found using a laser ceilometer. At the Reading University  
70 Atmospheric Observatory<sup>2</sup> (RUAO) located at 51.44136°N, 0.93807°W, a Chubb Instruments all-  
71 weather field mill, JCI131 is used, sampled at 1s intervals, co-located with a Vaisala CL31 ceilometer.  
72 The ceilometer determines the cloud base height to a resolution of 9m by a time-of-flight  
73 measurement from upward-propagating pulses of near infra-red laser light, together with a profile  
74 of the backscatter of the laser light up to cloud base. Little backscatter information is available  
75 within the cloud above the lower cloud-air boundary, as the CL31's laser light is strongly attenuated  
76 when it reaches the cloud. The Reading CL31 is configured to sample every 5 s, but subsequent  
77 samples cannot be regarded as entirely independent of each other as some smoothing and  
78 processing is applied by the manufacturer's internal algorithms (Kotthaus et al, 2016). Averages at  
79 one minute intervals are constructed for the first part of the analysis here, to both improve the

---

<sup>1</sup> The standard convention used here is that the Potential Gradient is  $-E_z$ , where  $E_z$  is the vertical component of the atmospheric electric field. The PG is positive in fair weather.

<sup>2</sup> <http://www.met.reading.ac.uk/observatorymain/>

1  
2  
3 80 vertical resolution and sample independence, with the 5 s raw data considered further in the second  
4  
5 81 part.

6  
7  
8 82 The RUAO also operates broadband radiation instruments to determine the solar radiation  
9  
10 83 components at the surface (including  $S_g$ , the global solar radiation and  $S_d$ , the diffuse component),  
11  
12 84 and the upwelling and downwelling longwave radiation ( $L_u$  and  $L_d$  respectively). Whilst 1s samples  
13  
14 85 are available for the solar radiation, the response time of the radiometer instruments themselves is  
15  
16 86 about 15s (Harrison, 2015). Further, during the period of the measurements discussed, the  $L_d$  values  
17  
18 87 were only available as 1 minute mean values.

19  
20  
21  
22 88 In addition, two instrumented balloon soundings were made. These used enhanced RS92  
23  
24 89 radiosondes, each carrying a pair of solar radiation sensors (Harrison et al, 2016). The characteristic  
25  
26 90 cloud-air transition in the solar radiation variability measured on a swinging radiosonde platform  
27  
28 91 (Nicoll and Harrison, 2012) was used to determine the cloud-top position.

29  
30  
31  
32 92 (b) *Conditions*

33 93 The layer-cloud investigated here persisted over RUAO during 19<sup>th</sup> March 2015 (year day 78 of 2015)  
34  
35 94 and dissipated after local noon on 20<sup>th</sup> March 2015. The cloud received unusually close scrutiny  
36  
37 95 because it obscured the partial solar eclipse which occurred on 20<sup>th</sup> March, and the associated  
38  
39 96 atmospheric electricity and meteorological conditions are extensively described in Bennett (2016)  
40  
41 97 and Burt (2016) respectively.

42  
43  
44  
45 98 Figure 1 shows ceilometer, PG and sounding measurements made beneath the layer-cloud. In  
46  
47 99 figure 1a, time series are given of the backscatter profile and the retrieved cloud base height, as  
48  
49 100 determined by the ceilometer's internal processing algorithm which uses the backscatter transition  
50  
51 101 at cloud base. During almost all of day 78, substantial and repeated fluctuations are evident in the  
52  
53 102 cloud base height, whereas for day 79, there is much less variability by comparison. (Images of the  
54  
55 103 cloud base on the two days are given in figure A1, to show the different appearance of the cloud  
56  
57  
58  
59  
60

1  
2  
3 104 base on the two days). Figure 1b presents the time series of PG beneath the cloud layer. It also  
4  
5 105 shows markedly more variability on day 78 compared with day 79.  
6  
7  
8 106 Radiosondes were released from RUAO at 0845 UTC on both days, and data from the two soundings  
9  
10 107 are shown in figures 1c and 1d and are summarised in Table 1. The soundings show thin cloud, of  
11  
12 108 thickness 323 m on day 78 and 432 m on day 79. Temperature inversions define the top of the cloud,  
13  
14 109 with the more marked inversion on day 79. Above the cloud at 800m, the relative humidity is 69%  
15  
16 110 (day 78) and 79% (day 79). A strong difference between the two days is the wind shear at the cloud-  
17  
18 111 top. For the day 78 sounding this exceeds  $0.1 \text{ s}^{-1}$  ( $(\text{m s}^{-1}) \text{ m}^{-1}$ ) in the 120m above the cloud-top,  
19  
20 112 whereas for the day 79 sounding it is much less,  $0.006 \text{ s}^{-1}$ . (Figures A1a and c provide skycam views  
21  
22 113 taken close to the balloon release times).  
23  
24  
25  
26

#### 27 114 *(c) Turbulence*

28 115 Horizontal wind shear is well-known to produce instability (Richardson 1920), which is apparent in  
29  
30 116 the generation of Kelvin-Helmholtz (K-H) waves made visible by cloud formation (Browning 1977).  
31  
32 117 These or related turbulent sources of regular motion, may therefore be driving the fluctuations  
33  
34 118 observed in the cloud base on day 78, which are not apparent on day 79 when the wind shear in the  
35  
36 119 sounding is negligible. This possibility is supported from examination of the hourly values of wind  
37  
38 120 speed and wind shear calculated by ECMWF (figures A2a and A2b), without assimilating the Reading  
39  
40 121 radiosonde data. Figure A2b shows that the strongest wind shear occurs at the same time as the  
41  
42 122 cloud base fluctuations. Direct comparison of the forecast with the radiosonde suggests that the  
43  
44 123 ECMWF model was better at predicting the mean horizontal wind speed than the wind shear and  
45  
46 124 therefore the exact location of the shear generating region, which is likely to be highly local, can only  
47  
48 125 be regarded as approximate.  
49  
50  
51  
52

53 126 The presence or absence of turbulence at the cloud-top can be assessed using the Richardson  
54  
55 127 number  $Ri$  (Richardson, 1920; Miles, 1961), found from the vertical gradients of potential  
56  
57 128 temperature  $\theta$  and horizontal wind speed components  $u$  and  $v$  as  
58  
59  
60



$$129 \quad Ri = \frac{g \frac{d\theta}{dz}}{\theta \left( \frac{du}{dz} \right)^2 + \left( \frac{dv}{dz} \right)^2} \quad (1),$$

130 where  $z$  is the height coordinate and  $g$  the gravitational acceleration. Turbulence is conventionally  
 131 regarded as present when  $Ri < 0.25$  (Miles 1961), although in some circumstances this threshold may  
 132 be larger (Zilitinkevich et al, 2008; Baklanov et al, 2011). Evaluating the vertical change in wind speed  
 133 and temperature over the transition distance of 120m evident at the cloud-top in figure 1c for both  
 134 days, Table 1 shows that  $Ri$  indicates turbulence at cloud-top on day 78 but not on day 79. Further  
 135 evidence that the variations in cloud base are associated with turbulence is provided from the power  
 136 spectrum of the cloud base height time samples (figure A2c), which also shows the Kolmogorov -5/3  
 137 spectral slope typical of a turbulent flow (Kolmogorov 1941).

138 For the case of K-H instability, which generates internal breaking waves from gravity waves (gravity-  
 139 restored displacements), a critical wavelength  $\lambda_c$  is identified by

$$140 \quad \lambda_c = \frac{\pi \rho (\Delta U)^2}{g \Delta T} \quad (2)$$

141 where the wind speed difference  $\Delta U$  and temperature  $\Delta T$  are evaluated cross the shear region and  $\rho$   
 142 is the air density (Cushman-Roison, 2014). Only gravity waves with wavelengths shorter than  $\lambda_c$  grow  
 143 into K-H billows. Table 1 also provides  $\lambda_c$  evaluated from equation (2) for both days using the  
 144 sounding information, from which it is apparent that K-H oscillations with wavelengths of tens of  
 145 metres are indicated to be possible on day 78.

146 The fluctuations in the cloud base apparent on day 78 can therefore be attributed to turbulent  
 147 motions generated by shear instability above the cloud top.

148

### 149 3. Observations of cloud fluctuations

150 The electrical variations associated with the dynamical instabilities are now considered further,

151 firstly for the slow periodic variations observed of the order of 10-20 minutes, and secondly for the  
 152 rapid steps that occurred on timescales of 1-2 minutes.

1  
2  
3 153 (a) *Slow symmetric fluctuations*

4 154 Figure 2a shows the detail of cloud base height and surface Potential Gradient (PG), from which it is  
5  
6 155 apparent that both quantities are well correlated. These slow fluctuations can be extracted by  
7  
8  
9 156 filtering, to remove variations with periods greater than 20 minutes. Figure 2b shows the same data  
10  
11 157 after high pass filtering from which the close, quasi-oscillatory relationship between the cloud base  
12  
13 158 height and PG is immediately evident. It is highly unusual to be able to identify the origin of surface  
14  
15 159 PG variability so explicitly, because multiple sources of variability are usually present. For the mean  
16  
17 160 cloud height in this case (483 m), cloud base height fluctuations of up to about  $\pm 70$  m are associated  
18  
19 161 with PG fluctuations of  $\pm 30$  V m<sup>-1</sup>. This sensitivity is larger than the typical 0.1 (Vm<sup>-1</sup>) m<sup>-1</sup> found  
20  
21 162 previously for slow cloud base changes (Harrison et al 2017a,b), suggesting that the charge varying in  
22  
23 163 this case is several times greater.

24  
25  
26  
27 164 Closer examination of the time series in figure 2b, however, indicates that the PG changes often  
28  
29 165 occur before the cloud base changes, i.e. that there is a lagged response. This adds weight to the  
30  
31 166 possibility that the responses observed are not solely due to cloud base fluctuations, instead, for  
32  
33 167 example, arising from vertical motion driven by the horizontal rolls above cloud top, combined with  
34  
35 168 local turbulence. This motivates further investigation of the lag. In figure 3, composites are formed  
36  
37 169 on the PG minima and maxima of the high pass filtered data to draw out the phasing of the PG and  
38  
39 170 cloud base changes. Two periods are chosen for this, the second quarter of day 78 (i.e. 78.25 to 78.5)  
40  
41 171 during which the radiosonde measurements of figure 1 were obtained and therefore when the shear  
42  
43 172 is observed to be present, and the second half of the day (i.e. 78.5 to 79), during which there were  
44  
45 173 larger fluctuations and the shear is inferred to continue from the ECMWF analysis. For both the PG  
46  
47 174 minima and maxima, statistically significant minima and maxima in the cloud base follow two  
48  
49 175 minutes later, with an in-phase response with the PG. This analysis verifies that the electrical  
50  
51 176 changes occur before the cloud base change observed by the ceilometer. The correlation  
52  
53 177 demonstrated in figure 2b is therefore not solely a result of vertical fluctuations in the position of  
54  
55 178 the charged cloud base, as these would cause an immediate response in the surface PG beneath.  
56  
57  
58  
59  
60

1  
2  
3 179 Some further insights into the cloud properties during the large cloud base height fluctuations can  
4  
5 180 be obtained by examining the solar radiation measurements beneath the cloud. Figure 4a and 4b  
6  
7 181 present cloud base and PG fluctuations, together with simultaneous co-located diffuse solar  
8  
9 182 irradiance ( $S_d$ ) measurements. Normalising the solar irradiance by the calculated (e.g. Harrison,  
10  
11 183 2015) top of atmosphere solar irradiance ( $S_{TOA}$ ) at the same time and high pass filtering, figure 4c  
12  
13 184 shows there is consistent behaviour in all three quantities during the latter half of the period  
14  
15 185 considered when there are large fluctuations. The good correlation between cloud base height and  
16  
17 186 solar radiation (shown in Table 2) for this period indicates that, when the cloud base rises and the PG  
18  
19 187 increases, the optical thickness of the cloud is reduced, i.e. considered overall, the cloud thins  
20  
21 188 significantly.

22  
23  
24  
25  
26 189 A similar timescale lag between changes in PG and radiation beneath a thin layer-cloud was found by  
27  
28 190 Harrison and Ambaum (2009). These new direct observations of changes at cloud base remove the  
29  
30 191 possible ambiguity of whether the previously reported effect arose from the cloud itself or through  
31  
32 192 modification to the radiation environment below it. Further, the similar lag time found both for  
33  
34 193 radiative instruments having a wide field of view and the ceilometer with a narrow point  
35  
36 194 measurement indicates that the lag does not originate from horizontal propagation of cloud base  
37  
38 195 anomalies which could affect the latter but not the former. Another physical length scale separating  
39  
40 196 the two changes is therefore implied, to allow time for propagation of a structure, for example  
41  
42 197 generated by a K-H wave, between the cloud top and bottom.

43  
44  
45  
46  
47 198 *(b) Rapid asymmetric fluctuations*

48 199 Further inspection of the cloud base height changes in figure 2b shows a range of amplitudes and  
49  
50 200 shapes, and not solely slow undulations as discussed above in section 3(a). To examine the  
51  
52 201 relationship between the electrical and cloud base changes more fully, all the rapid cloud base  
53  
54 202 changes from day 78 have been plotted against the instantaneous PG at the time of the cloud  
55  
56 203 change (figure 5), using the raw ceilometer data at 5s resolution. There are very many small cloud  
57  
58 204 base changes which provide the central region of data in figure 5a, associated with statistical  
59  
60

1  
2  
3 205 fluctuations between successive measurements, but there are also rather larger cloud base changes,  
4  
5 206 which are much rarer: these have been highlighted around the edges of the data in figure 5a. It is  
6  
7 207 clear that the distribution of these largest changes is asymmetric, in favour of positive (i.e. upwards)  
8  
9  
10 208 cloud base changes. Further, using boxplots to group the PG values associated with different rapid  
11  
12 209 cloud base changes (figure 5b), both negative and positive rapid cloud base changes with  
13  
14 210 magnitudes greater than 30m can be seen to be associated with an increased PG, compared with the  
15  
16 211 small cloud base changes.

18  
19 212 Figure 6 examines the detail of variations associated with typical rapid cloud base displacement  
20  
21 213 downwards (left hand columns) and upwards (right hand columns), again using the raw ceilometer  
22  
23 214 data at 5s resolution. In both cases shown the PG increases during the upward cloud base  
24  
25 215 displacement, as indicated by figure 5, but there are also associated changes in measurements of the  
26  
27 216 downwards longwave radiation (a decrease) and shortwave radiation (an increase). In the case of  
28  
29 217 the rapid upwards displacement, the upward fluctuations in cloud base recorded by the ceilometer  
30  
31 218 are associated with a reduction in longwave radiation due to cooling, and an increase in shortwave  
32  
33 219 radiation due to reduced optical thickness. The rapid change of cloud base position between  
34  
35 220 consecutive 5s samples is, in some ways, reminiscent of the step change in electric field seen for a  
36  
37 221 nearby lightning discharge.

38  
39 222 Figure 7 averages together (composites) all the rapid large (> 30m) upwards and downward  
40  
41 223 displacements in the raw 5s data of cloud base height, i.e. at 5 to 10 ms<sup>-1</sup>. The composites produce  
42  
43 224 the best summary of such changes, as they average many events together. These are for the same  
44  
45 225 period as that shown in figure 4, in which there are 51 downward displacements and 69 upwards  
46  
47 226 displacements. (This choice of step size is made so that it is several times greater than the minimum  
48  
49 227 ceilometer resolution of 9m, likely to arise from statistical fluctuations between successive  
50  
51 228 measurements.)  
52  
53  
54  
55  
56  
57  
58  
59  
60

1  
2  
3 229 In figure 7(a), the rapid downward displacement of cloud base at  $t=0$  in was preceded by a steady  
4  
5 230 upwards drift in cloud base height. This is a different behaviour from the rapid displacements at  $t=0$   
6  
7 231 in figure 7(d), in which there is effectively an isolated step change. In both the upward and  
8  
9 232 downward cases, however, the averaged PG increased steadily before the event, as seen in figure 5.  
10  
11 233 Notably, the PG reaches its maximum just before the cloud base decrease in figure 7a, and just after  
12  
13 234 the cloud base increase in figure 7d. The rapid upward and downward displacements are therefore  
14  
15 235 both generally associated with a prior increase in PG, and may be a consequence of the same  
16  
17 236 disturbance event. The composited backscatter values in (c) and (f) both show an increase in  
18  
19 237 backscatter at the displacement event time, with, necessarily, height variations before and after  
20  
21 238 similar to those of the cloud base ((a) and (d)) respectively. Consequently, the rapid upwards cloud  
22  
23 239 step is associated with displacing the dense backscatter region upwards.  
24  
25  
26  
27  
28 240 These additional composites in figure 7 indicate two aspects that need explanation. Firstly, the,  
29  
30 241 rapidity of the cloud steps, and secondly the PG increase for many minutes beforehand. The rapidity  
31  
32 242 is not what would be expected from a wavelike undulation in the cloud base, which would cause a  
33  
34 243 slow oscillation. Further, a simple propagating gap in the cloud base would lead to a PG change well  
35  
36 244 correlated with the cloud base change. However, in the composites, the shape of the onset and  
37  
38 245 recovery of the cloud base and PG changes are different.  
39  
40  
41  
42  
43

#### 4. Discussion

44 247  
45 248 Previous work has highlighted the close relationship between surface atmospheric electrical changes  
46  
47 249 and changes in the base of layer clouds, but in the observations reported here, electrical changes are  
48  
49 250 detected before a cloud base height change. In the case of the slow fluctuations, the observed time  
50  
51 251 lag is likely to be due to turbulence-induced downward motion of charge, based on the conclusions  
52  
53 252 of section 2 that cloud-top or above-cloud turbulence is generated during day 78, and of section 3a  
54  
55 253 that horizontal transport was unlikely. The presence of cloud-top charge, which in general is usually  
56  
57 254 greater than cloud base charge (Nicoll and Harrison, 2016), is indicated by the larger PG sensitivity to  
58  
59  
60

1  
2  
3 255 cloud base changes than previously observed. Overall, the scenario envisaged to explain the slow  
4  
5 256 symmetric variations with a lagged response is a dynamical disruption to the cloud-top charge which  
6  
7 257 is sensed immediately through an induced PG fluctuation at the surface, and that the effects of the  
8  
9 258 same disruption propagate to physically affect the cloud base some minutes later.  
10  
11  
12  
13 259 Beyond cloud-top disruption, if a region of positive charge were transported downwards by a wave  
14  
15 260 structure or billow, and there is no change in the cloud base charge, the surface PG will increase with  
16  
17 261 time as the charge descends. This may be apparent in figure 7b and 7d, in which a steady increase in  
18  
19 262 PG begins about 4 minutes before the cloud step occurs. With a descent speed  $W$  of  $0.5 \text{ ms}^{-1}$ , 120 m  
20  
21 263 would be travelled in this time, or about half of the cloud depth. For the charge to be retained  
22  
23 264 during its descent, the electrical conductivity must be sufficiently small for no appreciable  
24  
25 265 dissipation of the charge to occur. In air of conductivity  $\sigma$ , the relaxation timescale controlling its  
26  
27 266 discharge is  $\epsilon_0/\sigma$ , where  $\epsilon_0$  is the permittivity of free space. Hence, if the charge descends at a speed  
28  
29 267  $W$  through a cloud of conductivity  $\sigma_{\text{cloud}}$ , the time taken to pass through the cloud vertically must be  
30  
31 268 shorter than the relaxation time scale, for the charge to be maintained. This provides a solely  
32  
33 269 electrical condition on the maximum cloud depth  $D$ , as

$$D \ll \frac{W\epsilon_0}{\sigma_{\text{cloud}}} \quad (3)$$

37  
38 270  
39  
40  
41 271 assuming that there is no additional contribution to the discharge process from turbulent mixing.  
42  
43 272 The in-cloud conductivity is poorly known, but assuming  $\sigma_{\text{cloud}} \sim 2 \text{ fSm}^{-1}$  (i.e.  $\sim 1/5$ th of the typical  
44  
45 273 clear air conductivity at the surface) and  $W=0.5 \text{ ms}^{-1}$ , equation (3) requires that  $D$  should be less than  
46  
47 274 2212m, a condition which Table 1 indicates is easily fulfilled for the cloud circumstances described  
48  
49 275 and therefore that charge would be sustained during vertical transport.  
50  
51  
52  
53 276 More extensive evidence demonstrating downward motion in a similar thin layer-cloud on the same  
54  
55 277 day is available in data from Chilbolton, 55 km from Reading, where a ceilometer and an upwards-  
56  
57 278 facing Doppler cloud radar were both operating on day 78 of 2015. By compositing the Doppler  
58  
59  
60

279 radar data on the upwards cloud steps found from the Chilbolton ceilometer (figure A3), downward  
 280 motion (coloured blue, of about 0.2 to 0.5 m s<sup>-1</sup> beginning about 300m above the cloud base)  
 281 becomes apparent within the cloud before the cloud base step. This begins slightly before an  
 282 upwards cloud step, and is present through much of the vertical extent of the cloud after the step,  
 283 which, for the thin cloud during these conditions, is likely to include the upper charge region. (The  
 284 variability evident in the composite at about 400m above the cloud base is associated with the  
 285 cloud-top).

286 With this enhanced perspective from the Chilbolton data, the PG changes before an instantaneous  
 287 cloud step are now re-visited (figure 8a). This shows that the PG changes are not strongly correlated  
 288 with the cloud base before the cloud step, but afterwards they are more closely correlated. The pre-  
 289 step increase in PG is therefore not strongly associated with the cloud base. Downward propagation  
 290 of cloud-top charge, as observed at Chilbolton, is now considered as an explanation for the observed  
 291 pre-step PG increase. Electrostatic representation of layer clouds by simple models such as parallel  
 292 plate systems or point charges can only be regarded as approximate, but a disk charge model has  
 293 previously proved useful to represent cloud base charge, using charge densities typically ~ -1 nC m<sup>-2</sup>  
 294 on a disk of radius ~300 m (Harrison et al, 2017a). An assembly of positively charged droplets moving  
 295 from the cloud top has therefore been considered as a migrating disk charge. For a charged disk of  
 296 radius  $R$ , the electric field  $E$  at a distance  $H$  is derived from Gauss' Theorem as

$$297 \quad E = E_0 + \frac{Q}{2\pi\epsilon_0} \left[ 1 - \frac{H}{(H^2 + R^2)^{1/2}} \right] \quad (4),$$

298 where  $Q$  is the charge per unit area in the disk and  $E_0$  is the background field (Jackson, 1962). If  $H$  is  
 299 the height of the disk charge, the electric field (or PG as  $-E$ ) can be calculated beneath. Figure 8b  
 300 shows the calculated variation in the PG at the surface, for a +3 nCm<sup>-2</sup> disk charge of radius 200 m  
 301 descending from 500 m to 300 m altitude at 1 ms<sup>-1</sup>, as informed by figure A3. A background PG of  
 302 60 Vm<sup>-1</sup> is assumed in the absence of the disk charge, to represent the fair weather PG, itself likely to  
 303 be slightly suppressed by the presence of negative cloud base charge. Figure 8b shows agreement

1  
2  
3 304 between the averaged and calculated PG change, with a non-linear increase in surface PG associated  
4  
5 305 with the steady descent of the disk's positive charge. This indicates that the charge density and  
6  
7 306 dimensions assumed, following Harrison et al (2017a), are not unreasonable, and that the observed  
8  
9 307 PG increase before the cloud step is not inconsistent with a downward motion cloud top charge.  
10  
11  
12

### 13 308 14 309 **5. Conclusions**

15 310 A close electrical association between the cloud base charge in low-level extensive layer-clouds and  
16  
17 311 the surface PG has previously been established, using diurnal variations in cloud base height. Here,  
18  
19 312 cloud base variations are examined within a persistent layer-cloud which is sufficiently thin for shear  
20  
21 313 in the cloud-top to affect the cloud base. Observed surface electrical fluctuations are deduced to be  
22  
23 314 caused by instability at or above the cloud-top, generating a downwards-propagating disturbance  
24  
25 315 which ultimately reaches the cloud base, minutes later. Such a descent of charge from above can  
26  
27 316 provide a quantitatively reasonable physical explanation for the steady increase in PG observed prior  
28  
29 317 to more rapid cloud base changes.  
30  
31  
32

33  
34 318 This work demonstrates that atmospheric electrical properties are coupled with dynamical changes  
35  
36 319 within layer-clouds, rather than a constant electrostatic system. This, in principle offers a possible  
37  
38 320 method of remote sensing of cloud-top changes from the surface. It also illustrates, as the charge  
39  
40 321 transferred by the dynamical transport is carried on droplets, that regions of oppositely charged  
41  
42 322 droplets can be generated, locally modifying in-cloud electric fields. The interactions between  
43  
44 323 charged drops have previously been demonstrated to differ from those of neutral drops, for  
45  
46 324 example enhancing collision efficiencies and the timescale to produce rain. This may influence the  
47  
48 325 cloud lifetime, and therefore the break-up of the layer cloud, which is an important climate  
49  
50 326 parameter (Schneider et al, 2019). Further, as one region of charge is brought close to another of  
51  
52 327 opposite polarity, the possibility exists that intense local electric fields may be generated, ultimately  
53  
54 328 creating an electric discharge and generating radio frequency energy. Unexplained radio frequency  
55  
56 329 emissions have previously been reported from warm stratiform clouds (Sartor, 1964) and drizzle  
57  
58  
59  
60



1  
2  
3 330 producing clouds (Penzias and Wilson, 1970), for which the dynamically-forced transport of opposite  
4  
5 331 charges towards each other, causing a discharge, provides a possible mechanism.  
6  
7

8 332

9  
10 333  
11  
12  
13  
14  
15  
16  
17  
18  
19  
20  
21  
22  
23  
24  
25  
26  
27  
28  
29  
30  
31  
32  
33  
34  
35  
36  
37  
38  
39  
40  
41  
42  
43  
44  
45  
46  
47  
48  
49  
50  
51  
52  
53  
54  
55  
56  
57  
58  
59  
60

For Peer Review

1  
2  
3 334 **Appendix**  
4

5 335 Visual appearance of the cloud base can provide information on structure within a cloud and  
6  
7 336 characteristic features can sometimes be repeatedly identified (e.g. Harrison et al, 2017c). Sky  
8  
9 337 images are provided here for the days of interest from the Reading University Atmospheric  
10  
11 338 Observatory, captured using an AXIS Q6035 Dome Network Camera looking in a northward-pointing  
12  
13 339 direction. Figure A1 shows a series of images captured on 2015 day 78 ( (a) and (b) and day 79 ( (c)  
14  
15 340 and (d) ). More structure, although not strongly developed, is apparent on day 78 than on 79.  
16  
17  
18

19 341  
20  
21 342 [Figure A1]  
22

23 343  
24  
25 344 Additional information about the state of the lower atmosphere over Reading during 2015 days 78  
26  
27 345 and 79 is provided in figure A2, from the ECMWF high resolution forecast model. (a) shows the  
28  
29 346 ECMWF model output of the mean horizontal wind speed, (b) the time evolution of the wind shear  
30  
31 347 above Reading and (c) the relative spectral power density in the Reading cloud base observations. A  
32  
33 348 line showing a  $-5/3$  gradient of the spectral power against frequency, characteristic of turbulence, is  
34  
35 349 included.  
36  
37  
38

39 350  
40  
41 351 [Figure A2]  
42

43 352  
44  
45 353 The properties of the thin cloud on 2015 day 78 were also studied at Chilbolton, Hampshire, 55 km  
46  
47 354 from Reading were investigated using the Vaisala CL51 ceilometer sited there, which operates in the  
48  
49 355 same way as the CL31 device at Reading. At Chilbolton there is also an upward-pointing Doppler  
50  
51 356 radar (Copernicus) able to determine the speed of the cloud particles upwards or downwards.  
52  
53 357 Figure A3 shows an average of the cloud particle speeds, around the times of rapid upward steps in  
54  
55 358 the cloud base as determined by the ceilometer. The cloud particle speeds are shown spatially, with  
56  
57 359 respect to the cloud base position found by the ceilometer. The variability in the upper part of the  
58  
59  
60

1  
2  
3 360 plot is associated with the cloud top. At the time of the cloud step, the Doppler radar shows that  
4  
5 361 there is descending air within the cloud.  
6  
7

8 362

9  
10 363 [Figure A3]  
11

12 364

13  
14 365 **Acknowledgements**

15 366 K.A.N. acknowledges NERC support through an Independent Research Fellowship (NE/L011514/1

16  
17 367 and NE/L011514/2). The Copernicus Radar data and ceilometer data at Chilbolton used in figure A3

18  
19 368 was provided by Chris Westbrook. The ECMWF forecast model data was obtained from the ECMWF

20  
21 369 MARS archive. Ken Bignell provided valuable information about the static discharges associated with

22  
23 370 non-thunderstorm clouds. The original data used is available from the corresponding author.  
24  
25

26  
27 371  
28  
29  
30  
31  
32  
33  
34  
35  
36  
37  
38  
39  
40  
41  
42  
43  
44  
45  
46  
47  
48  
49  
50  
51  
52  
53  
54  
55  
56  
57  
58  
59  
60

372 **References**

- 373 Baklanov A, Grisogono B, Bornstein R, Mahrt L, Zilitinkevich S, Taylor P, Larsen S, Rotach M, and  
374 Fernando H, 2011. On the nature, theory, and modeling of atmospheric planetary boundary layers  
375 *Bulletin of the American Meteorological Society*. 92, 2, 123-128.
- 376 Bennett, AJ. 2016. Effects of the March 2015 solar eclipse on near-surface atmospheric electricity.  
377 *Phil. Trans. R. Soc. Lond A*, 374(2077), 2015.
- 378 Browning, KA. 1971. Structure of the atmosphere in the vicinity of large-amplitude Kelvin-Helmholtz  
379 billows. *Quart Jour Roy Meteor Soc*, 97, 413, 283-299
- 380 Burt, S. 2016. Meteorological responses in the atmospheric boundary layer over southern England to  
381 the deep partial eclipse of 20 March 2015. *Phil. Trans. R. Soc Lond. A*, 374(2077), 20150214.
- 382 Cushman-Roisin, B. 2014. *Environmental Fluid Dynamics*, Online book,  
383 <http://www.dartmouth.edu/~cushman/books/EFM.html>
- 384 Harrison RG. 2015. *Meteorological measurements and instrumentation*, (Wiley).
- 385 Harrison RG, MHP Ambaum. 2008. Enhancement of cloud formation by droplet charging. *Proc. R.*  
386 *Soc. Lond A*. **464**: 2561–2573.
- 387 Harrison RG, MHP Ambaum, 2009. Observed atmospheric electricity effect on clouds, *Environ. Res.*  
388 *Lett.* **4** 014003
- 389 Harrison RG, GJ Marlton, PD Williams, KA Nicoll. 2016. Coordinated weather balloon solar radiation  
390 measurements during a solar eclipse, *Phil Trans Roy Soc Lond A* 374, 20150221  
391 (doi:10.1098/rsta.2015.0221)
- 392 Harrison, RG, KA Nicoll, KL Aplin. 2017a. Evaluating stratiform cloud base charge remotely, *Geophys*  
393 *Res Lett*, 44, 10.1002/2017GL073128
- 394 Harrison, RG, KA Nicoll, KL Aplin, 2017b. Remote sensing of cloud base charge. Proc 2017 meeting of  
395 Electrostatics Society of America, University of Ottawa, June 2017. <https://arxiv.org/abs/1705.05689>
- 396 Harrison, RG and KA Nicoll, 2018. Fair weather criteria for atmospheric electricity measurements  
397 *J Atmos Sol-terr phys* 179, 239-250 <https://doi.org/10.1016/j.jastp.2018.07.008>

- 1  
2  
3 398 Harrison, RG, G Pretor-Pinney, GJ Marlton, GD Anderson, DJ Kirshbaum, RJ Hogan, 2017c. Asperitas –  
4  
5 399 a newly identified cloud supplementary feature, *Weather* 72 (May 2017), 5, 132-141.  
6  
7 400 Jackson, D, 1962. *Classical Electrodynamics*, Wiley  
8  
9 401 Khain A, V Arkhipov, M Pinsky, Y Feldman, Y Ryabov. 2004. Rain enhancement and fog elimination by  
10  
11 402 seeding with charged droplets. Part I: Theory and numerical simulations. *J. Appl. Meteorol.* 43: 1513–  
12  
13 403 1529.  
14  
15 404 Klein SA, Hartmann DL. 1993. The seasonal cycle of low stratiform clouds. *J. Clim.* 6: 1587–1606.  
16  
17 405 Kolmogorov, AN, 1941. The local structure of turbulence in incompressible viscous fluid for very  
18  
19 406 large Reynolds numbers, *Dokl. Akad. Nauk SSSR*, 30(4), pp301--305  
20  
21 407 Kotthaus S. et al. 2016. Recommendations for processing atmospheric attenuated backscatter  
22  
23 408 profiles from Vaisala CL31 ceilometers *Atmos. Meas. Tech.*, 9, 3769–3791  
24  
25 409 Miles, JW. 1961. On the stability of heterogeneous shear flows, *J. Fluid Mech*, 10(4), 496-508  
26  
27 410 Nicoll KA, Harrison RG. 2016. Stratiform cloud electrification: comparison of theory with multiple in-  
28  
29 411 cloud measurements *Quart Jour Roy Meteor Soc* 142, 2679–2691 (2016) 10.1002/qj.2858  
30  
31 412 Nicoll KA, Harrison RG. 2012. Balloon-borne disposable radiometer for cloud detection. *Rev. Sci.*  
32  
33 413 *Instrum.* 83: 025111  
34  
35 414 Penzias, AA, RW Wilson, 1970. Microwave noise from rainstorms. *Science*. 169 (3945) 583-584.  
36  
37 415 Richardson, LF. 1920. The supply of energy from and to atmospheric eddies, *Proc Royal Soc Lond. A*,  
38  
39 416 97(686), 354-373  
40  
41 417 Sartor JD, 1964. Radio observation of the electromagnetic emission from warm clouds. *Science* 143,  
42  
43 418 (3609) 948-949.  
44  
45 419 Schneider T, Kaul, CM, Pressel, KG, 2019. Possible climate transitions from breakup of stratocumulus  
46  
47 420 decks under greenhouse warming *Nature Geosci* 12, 163–167 10.1038/s41561-019-0310-1  
48  
49 421 Shao Q, DA Randal, CH Moeng and RE Dickinson, 1997. A method to determine the amounts of  
50  
51 422 cloud-top radiative and evaporative cooling in a stratocumulus-topped boundary layer, *Quart Jour*  
52  
53 423 *Roy Meteor Soc*, 123(544), 2187--2213  
54  
55  
56  
57  
58  
59  
60

- 1  
2  
3 424 Tinsley BA, RP Rohrbaugh, M Hej, KV Beard. 2000. Effects of image charges on the scavenging of  
4  
5 425 aerosol particles by cloud droplets and on droplet charging and possible ice nucleation processes. *J.*  
6  
7 426 *Atmos. Sci.* **57**:2118–2134.  
8  
9  
10 427 Zhou L, BA Tinsley. 2012. Time dependent charging of layer clouds in the global electric circuit. *Adv.*  
11  
12 428 *Space Res.* **506**: 828–842.  
13  
14 429 Zilitinkevich SS., Elperin T, Kleerorin N, Rogachevskii I, Esau I, Mauritsen T and Miles, MW., 2008.  
15  
16 430 Turbulence energetics in stably stratified geophysical flows: Strong and weak mixing regimes *Quart*  
17  
18 431 *Jour Roy Meteor Soc* 134, 793–799 DOI: 10.1002/qj.264  
19  
20  
21 432  
22 433  
23  
24  
25  
26  
27  
28  
29  
30  
31  
32  
33  
34  
35  
36  
37  
38  
39  
40  
41  
42  
43  
44  
45  
46  
47  
48  
49  
50  
51  
52  
53  
54  
55  
56  
57  
58  
59  
60

For Peer Review

1  
2  
3 **434 Figure captions and Tables**

4 435  
5 436 Figure 1. Time series of (a) backscatter obtained from a CL31 laser ceilometer above Reading on 19<sup>th</sup>  
6  
7 437 and 20<sup>th</sup> March 2015 (year days 78 and 79), with the instrument-retrieved cloud base marked in  
8  
9 438 black. (b) Time series of electric potential gradient (PG) measured at the surface. Dashed lines mark  
10  
11 439 times of radiosonde launches. Sounding profiles obtained are shown in (c) and (d), of air  
12  
13 440 temperature ( $T_{air}$ , black line) and dewpoint temperature ( $T_{dew}$ , grey line) and horizontal wind speed  
14  
15 441 ( $U$ , green dots). The cloud base and top are marked with horizontal lines. (The cloud base is obtained  
16  
17 442 from the ceilometer, and the cloud top from a solar radiation sensor carried on the radiosondes,  
18  
19 443 with cloud top defined as the position where measured solar radiation variability is halfway between  
20  
21 444 its in-cloud and clear air values).  
22  
23  
24  
25  
26  
27

28 446 Figure 2. Time series of cloud base height (thin black line) and surface Potential Gradient (PG, thick  
29  
30 447 red line), as (a) 1 minute mean values and (b) high pass filtered 1 minute values, with variations  
31  
32 448 slower than 20 minutes removed.  
33  
34  
35  
36

37 450 Figure 3. Averages of cloud base height fluctuations (black lines), calculated (composited) during the  
38  
39 451 second quarter (a and b) and second half (c and d) of day 78, in both case on minima (a and c) and  
40  
41 452 maxima (b and d) in the PG, using 1 minute high pass filtered values. The associated averages of  
42  
43 453 changes in the PG values are also shown (red lines). Grey bands show the 95% confidence range on  
44  
45 454 the cloud base values, from repeated sampling of the same number of events, but not associated  
46  
47 455 with PG maxima and minima.  
48  
49

50 456  
51  
52 457 Figure 4. Selected time series of (a) backscatter and cloud base (black line), (b) PG (red line) and  
53  
54 458 diffuse solar radiation ( $S_d$ , blue dashed line). (c) Time series of high pass filtered time series of cloud  
55  
56 459 base (black line), solar radiation normalised by calculated top of atmosphere value at the same time  
57  
58 460 ( $S_d/S_{TOA}$ , blue dashed line) and cloud base (black line). (Data are 1min averages from 1s samples.)  
59  
60

461

462 Figure 5. Cloud base changes on day 78 plotted against the instantaneous PG at the time of the  
 463 change (ceilometer resolution 9m, 5s samples). (a) All cases, with the extreme values emphasised by  
 464 increasing the size of the plotted point and its grayscale density in proportion to the cloud base  
 465 change. (b) Cloud base changes from (a) binned into steps of 0 to  $\pm 30\text{m}$ ,  $\pm 30$  to  $\pm 60\text{m}$  and  $> \pm 60\text{m}$ ,  
 466 shown as boxplots with the number of cases marked.

467

468 Figure 6. Changes associated with instantaneous fluctuation in the cloud base, downwards (left  
 469 column) and upwards (right column). (a) and (d) show backscatter profiles and cloud base position  
 470 (black line with points), (b) and (e) cloud base (black line with points) and PG (red line), (c) and (f),  
 471 diffuse and global solar radiation ( $S_g$  and  $S_d$ ), and downwards long wave radiation ( $L_d$ ). The  
 472 ceilometer provides 5s data and the PG,  $S_d$ ,  $S_g$  are 1s values,  $L_d$  are 1 min values.

473

474 Figure 7. Composites between days 78.4 and 78.7 of variation in mean vertical position of cloud base  
 475 using the instantaneous data ( (a) and (d) ), ( (b) and (e) ) mean surface potential gradient, and ( (c)  
 476 and (f) ) median backscatter, reckoned from cloud base height at the event time. For (a)-(d) the 95%  
 477 confidence on the line is marked. Left-hand panels are for rapid cloud base height decreases, and  
 478 right-hand panels are for cloud base increases, with time axes all in minutes.

479

480 Figure 8. (a) Overlaid composites of cloud base (grey line and points, left-hand axis) and surface PG  
 481 (red line, right-hand axis), from figs 7d and 7e. (b) Composited surface PG observations from (a),  
 482 (solid red line, with 95% confidence limits dotted). The calculated surface PG is also included (black  
 483 solid line), found from assuming a horizontal charged disk of radius 200 m carrying a charge density  
 484 of  $+3 \text{ nC m}^{-2}$ , descending at  $1 \text{ ms}^{-1}$  from 500 m to 300 m, in a background surface PG of  $60 \text{ Vm}^{-1}$ . The  
 485 variation of the disk charge position with time is given by the black dashed line (right-hand axis).

486



1  
2  
3 487 Figure A1. Skycam views northwards from the Reading University Atmospheric Observatory, on 19th  
4  
5 488 March 2015 at (a) 0910 and (b) 1525, and 20th March 2015 at (c) 0911 and 1114.  
6  
7  
8 489

9  
10 490 Figure A2. (a) and (b) time-height plots from the ECMWF high resolution forecast model. These are  
11  
12 491 for the Reading grid square at 1 hour time steps, between the beginning of day 78 and the end of  
13  
14 492 day 79, using forecasts initiated at midday and midnight. (a) mean horizontal wind speed ( $U$ ) and (b)  
15  
16 493 vertical wind shear ( $dU/dz$ ), with the ceilometer cloud base measurements from Reading added to  
17  
18 494 (a) (black line). (c) Relative power spectral density (PSD) calculated from the high pass filtered  
19  
20 495 1 minute cloud base height measurements, for the period of the cloud base fluctuations in day 78  
21  
22 496 (78.25 to 79). The dashed line marks a spectral slope of  $-5/3$ .  
23  
24  
25

26 497 Figure A3. Analysis of layer cloud properties at Chilbolton during day 78 of 2015, by combining data  
27  
28 498 from the site's laser ceilometer and cloud radar. The plot shows the averaged Doppler radar velocity  
29  
30 499 within the cloud at a ceilometer upwards step, composited from 12 upwards cloud fluctuations  
31  
32 500 exceeding 35m in the ceilometer data. The changes are found for the first 29 radar range gates  
33  
34 501 above the mean cloud base height as found by the ceilometer,  $\pm 15$  minutes across each  $>35$ m step.  
35  
36 502 (Blue colours show vertically downward wind directions.)  
37  
38  
39  
40 503  
41  
42 504  
43  
44  
45  
46  
47  
48  
49  
50  
51  
52  
53  
54  
55  
56  
57  
58  
59  
60

**Table 1. Properties derived from the two atmospheric soundings**

Day of 2015	Cloud parameters			Cloud top gradients*		Turbulence parameters	
	Ceilometer cloud base at launch (m)	Cloud top height (m)	Cloud depth (m)	Wind shear ((ms <sup>-1</sup> )m <sup>-1</sup> )	Temperature change (K m <sup>-1</sup> )	Richardson number Ri	critical wavelength $\lambda_c$ (m)
78 (19 <sup>th</sup> March)	318	641	323	0.11	0.015	0.04	38
79 (20 <sup>th</sup> March)	218	650	432	0.006	0.032	0.6	0.06

\*calculated across 120m layer at cloud top

**Table 2. Pearson correlations between filtered variables from figure 4(c).**

<i>Day fraction</i>	78.4 to 78.55	78.55 to 78.7
<i>Variables</i>		
Cloud base height and ( $S_d/S_{TOA}$ )	0.02	0.37
PG and ( $S_d/S_{TOA}$ )	0.37	0.71

For Peer Review

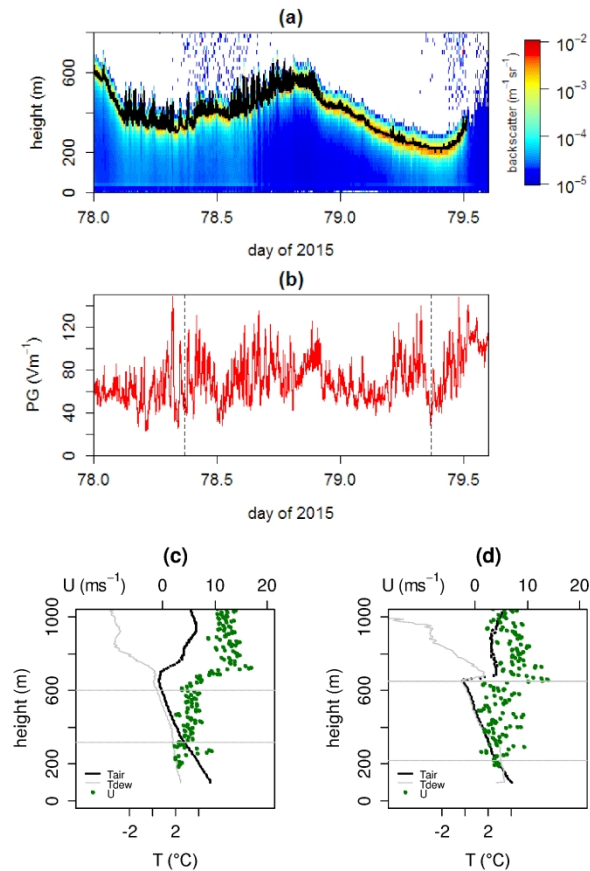


Figure 1. Time series of (a) backscatter obtained from a CL31 laser ceilometer above Reading on 19th and 20th March 2015 (year days 78 and 79), with the instrument-retrieved cloud base marked in black. (b) Time series of electric potential gradient (PG) measured at the surface. Dashed lines mark times of radiosonde launches. Sounding profiles obtained are shown in (c) and (d), of air temperature ( $T_{air}$ , black line) and dewpoint temperature ( $T_{dew}$ , grey line) and horizontal wind speed ( $U$ , green dots). The cloud base and top are marked with horizontal lines. (The cloud base is obtained from the ceilometer, and the cloud top from a solar radiation sensor carried on the radiosondes, with cloud top defined as the position where measured solar radiation variability is halfway between its in-cloud and clear air values).

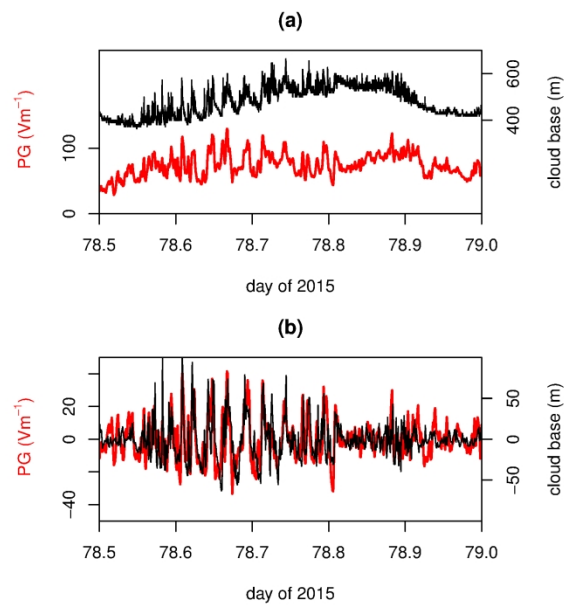


Figure 2. Time series of cloud base height (thin black line) and surface Potential Gradient (PG, thick red line), as (a) 1 minute mean values and (b) high pass filtered 1 minute values, with variations slower than 20 minutes removed.

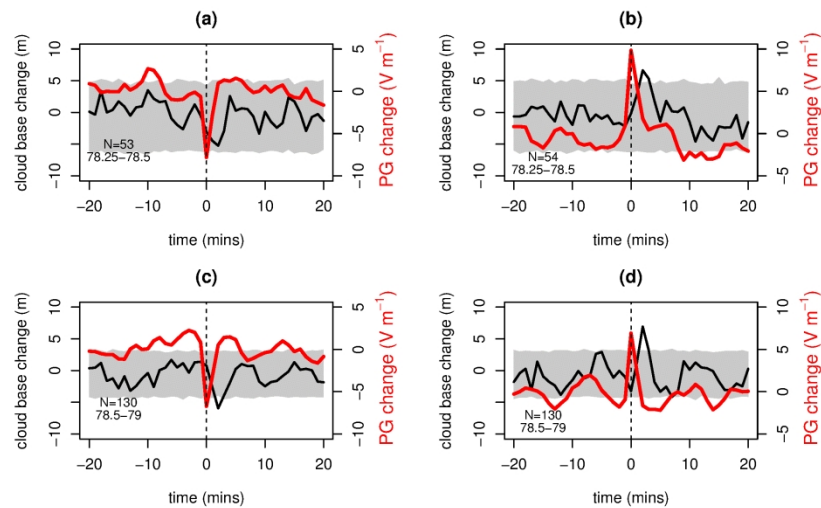


Figure 3. Averages of cloud base height fluctuations (black lines), calculated (composited) during the second quarter (a and b) and second half (c and d) of day 78, in both case on minima (a and c) and maxima (b and d) in the PG, using 1 minute high pass filtered values. The associated averages of changes in the PG values are also shown (red lines). Grey bands show the 95% confidence range on the cloud base values, from repeated sampling of the same number of events, but not associated with PG maxima and minima.

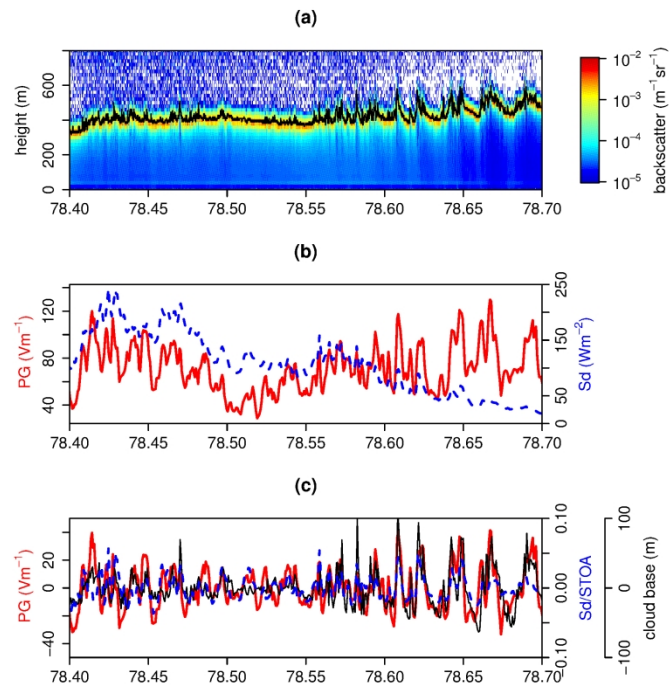


Figure 4. Selected time series of (a) backscatter and cloud base (black line), (b) PG (red line) and diffuse solar radiation (Sd, blue dashed line). (c) Time series of high pass filtered time series of cloud base (black line), solar radiation normalised by calculated top of atmosphere value at the same time (Sd/STOA, blue dashed line) and cloud base (black line). (Data are 1min averages from 1s samples.)

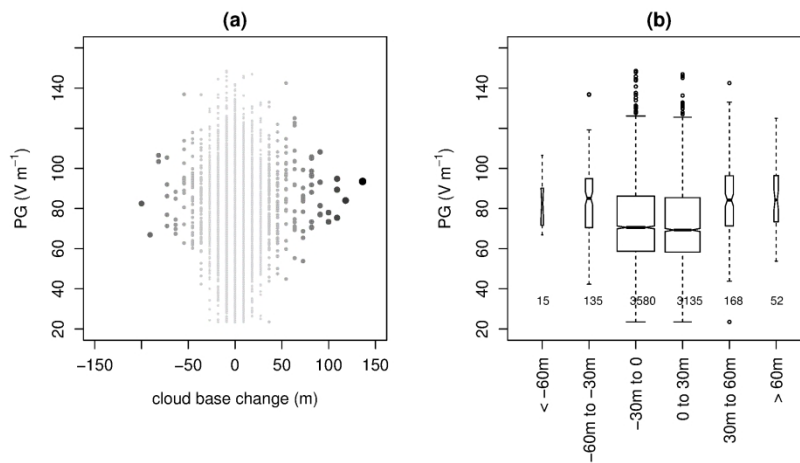


Figure 5. Cloud base changes on day 78 plotted against the instantaneous PG at the time of the change (ceilometer resolution 9m). (a) All cases, with the extreme values emphasised by increasing the size of the plotted point and its grayscale density in proportion to the cloud base change. (b) Cloud base changes from (a) binned into steps of 0 to  $\pm 30$ m,  $\pm 30$  to  $\pm 60$ m and  $> \pm 60$ m, shown as boxplots with the number of cases marked.



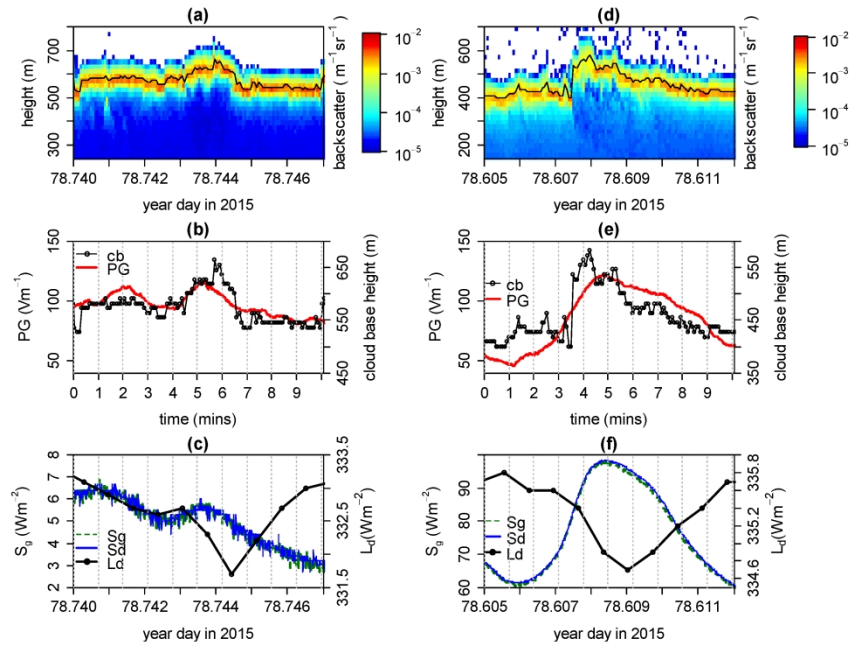


Figure 6. Changes associated with instantaneous fluctuation in the cloud base, downwards (left column) and upwards (right column). (a) and (d) show backscatter profiles and cloud base position (black line with points), (b) and (e) cloud base (black line with points) and PG (red line), (c) and (f), diffuse and global solar radiation (S<sub>g</sub> and S<sub>d</sub>), and downwards long wave radiation (L<sub>d</sub>). The ceilometer provides 5s data and the PG, S<sub>d</sub>, S<sub>g</sub> are 1s values, L<sub>d</sub> are 1 min values.

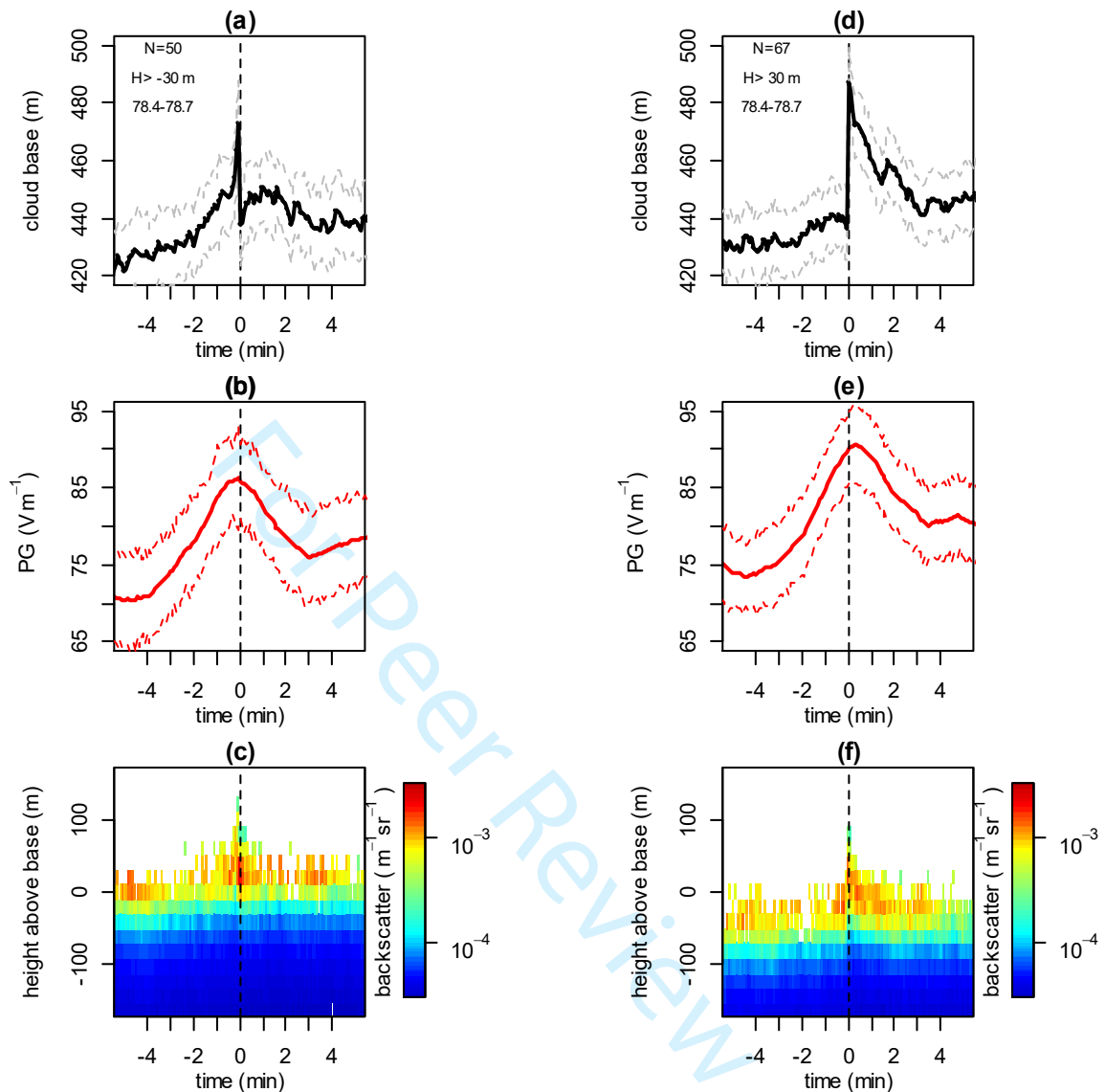


Figure 7. Composites between days 78.4 and 78.7 of variation in mean vertical position of cloud base using the instantaneous data ( (a) and (d) ), ( (b) and (e) ) mean surface potential gradient, and ( (c) and (f) ) median backscatter, reckoned from cloud base height at the event time. For (a)-(d) the 95% confidence on the line is marked. Left-hand panels are for rapid cloud base height decreases, and right-hand panels are for cloud base increases, with time axes all in minutes.

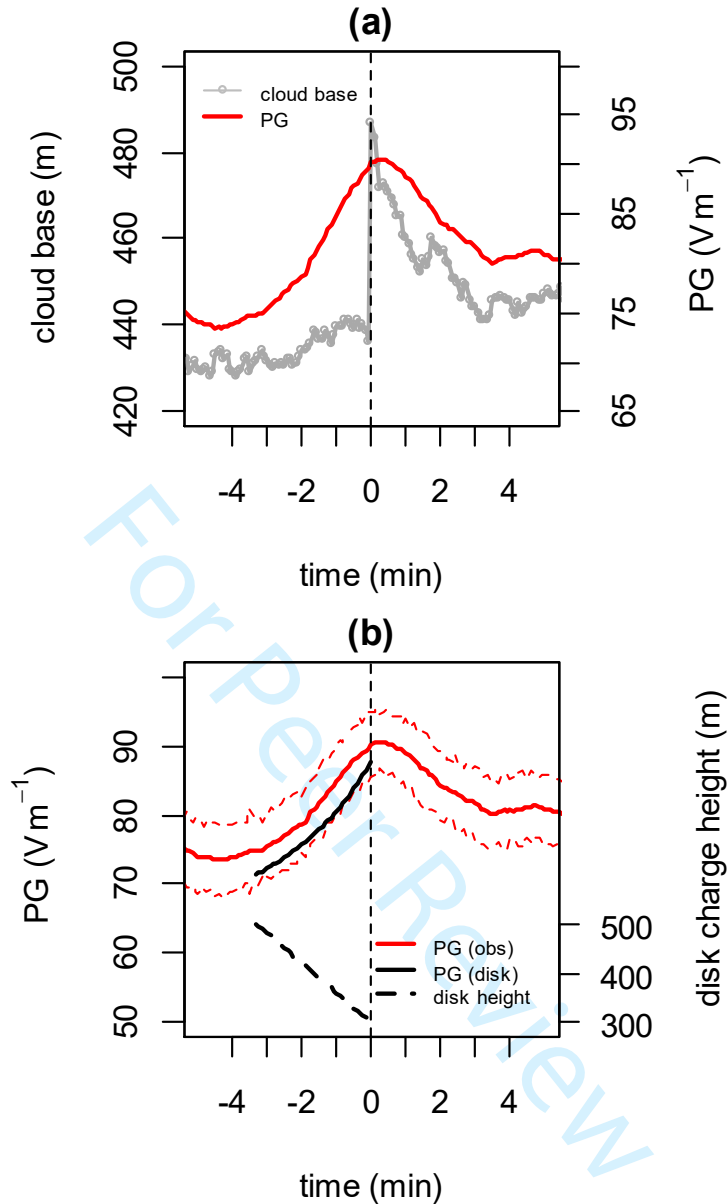


Figure 8. (a) Overlaid composites of cloud base (grey line and points, left-hand axis) and surface PG (red line, right-hand axis), from figs 7d and 7e. (b) Composites of surface PG observations from (a), (solid red line, with 95% confidence limits dotted). The calculated surface PG is also included (black solid line), found from assuming a horizontal charged disk of radius 200 m carrying a charge density of  $+3 \text{ nC m}^{-2}$ , descending at  $1 \text{ ms}^{-1}$  from 500 m to 300 m, in a background surface PG of  $60 \text{ V m}^{-1}$ . The variation of the disk charge position with time is given by the black dashed line (right-hand axis).

1  
2  
3  
4  
5  
6  
7  
8  
9  
10  
11  
12  
13  
14  
15  
16  
17  
18  
19  
20  
21  
22  
23  
24  
25  
26  
27  
28  
29  
30  
31  
32  
33  
34  
35  
36  
37  
38  
39  
40  
41  
42  
43  
44  
45  
46  
47  
48  
49  
50  
51  
52  
53  
54  
55  
56  
57  
58  
59  
60

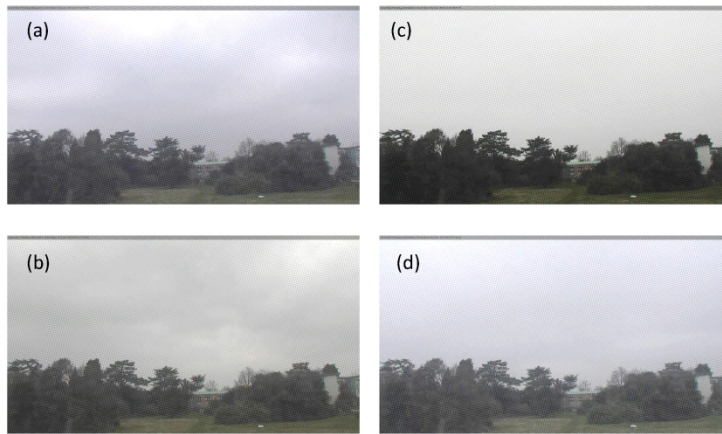


Figure A1. Skycam views northwards from the Reading University Atmospheric Observatory, on 19th March 2015 at (a) 0910 and (b) 1525, and 20th March 2015 at (c) 0911 and 1114.

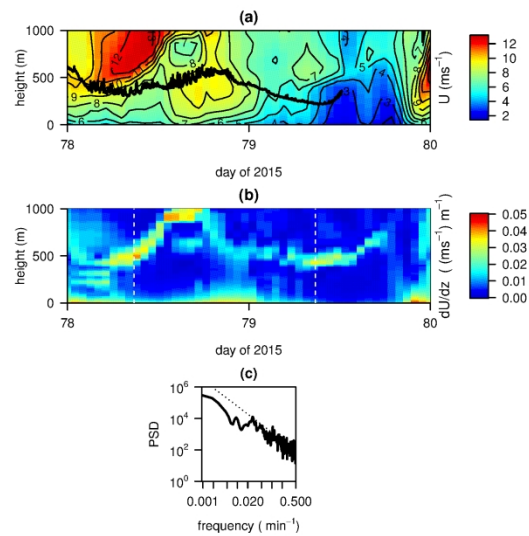


Figure A2. (a) and (b) time-height plots from the ECMWF high resolution forecast model. These are for the Reading grid square at 1 hour time steps, between the beginning of day 78 and the end of day 79, using forecasts initiated at midday and midnight. (a) mean horizontal wind speed ( $U$ ) and (b) vertical wind shear ( $dU/dz$ ), with the ceilometer cloud base measurements from Reading added to (a) (black line). (c) Relative power spectral density (PSD) calculated from the high pass filtered 1 minute cloud base height measurements, for the period of the cloud base fluctuations in day 78 (78.25 to 79). The dashed line marks a spectral slope of  $-5/3$ .

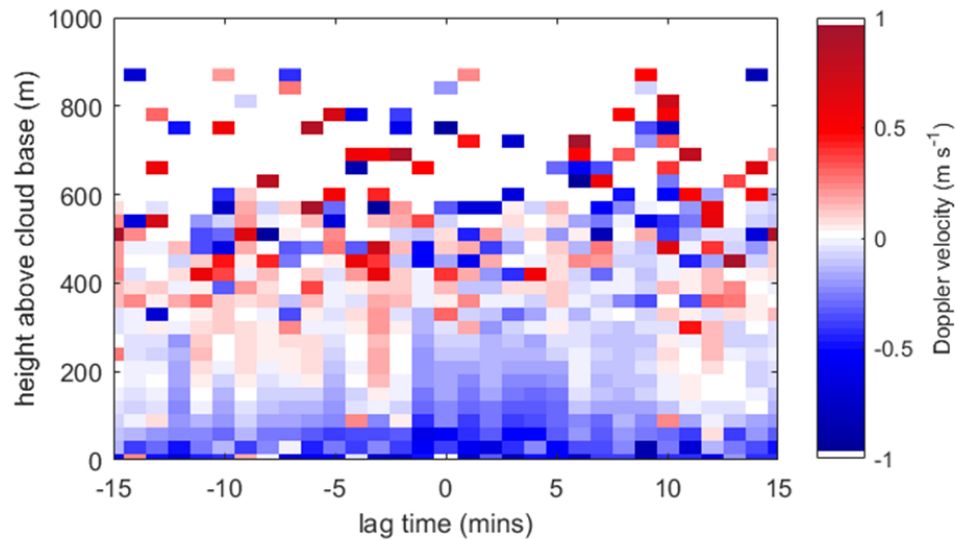


Figure A3. Analysis of layer cloud properties at Chilbolton during day 78 of 2015, by combining data from the site's laser ceilometer and cloud radar. The plot shows the averaged Doppler radar velocity within the cloud at a ceilometer upwards step, composited from 12 upwards cloud fluctuations exceeding 35m in the ceilometer data. The changes are found for the first 29 radar range gates above the mean cloud base height as found by the ceilometer,  $\pm 15$  minutes across each  $>35\text{m}$  step. (Blue colours show vertically downward wind directions.)

## Shear-induced electrical changes in the base of thin layer-cloud

R. Giles Harrison\*, Graeme J. Marlton, Karen L. Aplin, Keri A. Nicoll

Extensive layer clouds accumulate charge naturally at their upper and lower boundaries. Fluctuations observed in the base of a thin layer cloud are found to be closely correlated with the atmospheric electric Potential Gradient at the surface, indicating charge transport. Measurements from Reading University Observatory on 19<sup>th</sup> March 2015 (day 78 of 2015) show (a) ceilometer backscatter and (b) fluctuations in the atmospheric electrical Potential Gradient (thick red line) and cloud base height (thin black line).

